Research Article | Vol. 7, No. 8 | 1 Aug 2016 | BIOMEDICAL OPTICS EXPRESS 3056
Biomedical Optics EXPRESS

Synthetic-aperture based photoacoustic re-beamforming (SPARE) approach using beamformed ultrasound data

HAICHONG K. ZHANG,[1,4] MUYINATU A. LEDIJU BELL,[1,2] XIAOYU GUO,[2] HYUN JAE KANG,[1] AND EMAD M. BOCTOR[1,2,3,5]

[1]*Department of Computer Science, The Johns Hopkins University, Baltimore, Maryland, 21218, USA*
[2]*Department of Electrical and Computer Engineering, The Johns Hopkins University, Baltimore, Maryland, 21218, USA*
[3]*Department of Radiology, The Johns Hopkins Medical Institue, Baltimore, Maryland, 21213, USA*
[4]*hzhang61@jhu.edu*
[5]*eboctor1@jhmi.edu*

Abstract: Photoacoustic (PA) imaging has been developed for various clinical and pre-clinical applications, and acquiring pre-beamformed channel data is necessary to reconstruct these images. However, accessing these pre-beamformed channel data requires custom hardware to enable parallel beamforming, and is available for a limited number of research ultrasound platforms. To broaden the impact of clinical PA imaging, our goal is to devise a new PA reconstruction approach that uses ultrasound post-beamformed radio frequency (RF) data rather than raw channel data, because this type of data is readily available in both clinical and research ultrasound systems. In our proposed Synthetic-aperture based photoacoustic re-beamforming (SPARE) approach, post-beamformed RF data from a clinical ultrasound scanner are considered as input data for an adaptive synthetic aperture beamforming algorithm. When receive focusing is applied prior to obtaining these data, the focal point is considered as a virtual element, and synthetic aperture beamforming is implemented assuming that the photoacoustic signals are received at the virtual element. The resolution and SNR obtained with the proposed method were compared to that obtained with conventional delay-and-sum beamforming with 99.87% and 91.56% agreement, respectively. In addition, we experimentally demonstrated feasibility with a pulsed laser diode setup. Results indicate that the post-beamformed RF data from any commercially available ultrasound platform can potentially be used to create PA images.

OCIS codes: (170.5120) Photoacoustic imaging; (100.0100) Image processing; (100.3010) Image reconstruction techniques.

References and links

1. M. Xu and L. V. Wang, "Photoacoustic imaging in biomedicine," Rev. Sci. Instrum. **77**(4), 041101 (2006).
2. S. Park, S. R. Aglyamov, and S. Emelianov, "Beamforming for photoacoustic imaging using linear array transducer," Proc. in IEEE Int. Ultrasonics Symp., 856–859 (2007).
3. B. Yin, D. Xing, Y. Wang, Y. Zeng, Y. Tan, and Q. Chen, "Fast photoacoustic imaging system based on 320-element linear transducer array," Phys. Med. Biol. **49**(7), 1339–1346 (2004).
4. C. K. Liao, M. L. Li, and P. C. Li, "Optoacoustic imaging with synthetic aperture focusing and coherence weighting," Opt. Lett. **29**(21), 2506–2508 (2004).
5. R. G. M. Kolkman, P. J. Brands, W. Steenbergen, and T. G. van Leeuwen, "Real-time in vivo photoacoustic and ultrasound imaging," J. Biomed. Opt. **13**(5), 050510 (2008).
6. J. J. Niederhauser, M. Jaeger, and M. Frenz, "Comparision of laser-induced and classical ultrasound," Proc. SPIE **4960**, 118–123 (2003).
7. N. Kuo, H. J. Kang, D. Y. Song, J. U. Kang, and E. M. Boctor, "Real-time photoacoustic imaging of prostate brachytherapy seeds using a clinical ultrasound system," J. Biomed. Opt. **17**(6), 066005 (2012).
8. H. J. Kang, N. Kuo, X. Guo, D. Song, J. U. Kang, and E. M. Boctor, "Software framework of a real-time pre-beamformed RF data acquisition of an ultrasound research scanner," Proc. SPIE **8320**, 83201F (2012).
9. T. Harrison and R. J. Zemp, "The applicability of ultrasound dynamic receive beamformers to photoacoustic imaging," IEEE Trans. Ultrason. Ferroelectr. Freq. Control **58**(10), 2259–2263 (2011).

#264984 http://dx.doi.org/10.1364/BOE.7.003056
Journal © 2016 Received 11 May 2016; revised 17 Jun 2016; accepted 29 Jun 2016; published 19 Jul 2016

Biomedical Optics EXPRESS

10. C. H. Frazier and W. D. O'Brien, "Synthetic aperture techniques with a virtual source element," IEEE Trans. Ultrason., Ferroelec, Freq. Contr. **45**(1), 196–207 (1998).
11. S. I. Nikolov and J. A. Jensen, "Virtual ultrasound sources in high resolution ultrasound imaging," Proc. SPIE, Progress in biomedical optics and imaging, **3**, 395–405 (2002).
12. J. Kortbek, J. A. Jensen, and K. L. Gammelmark, "Synthetic Aperture Sequential Beamforming," Proc. in IEEE Int. Ultrasonics Symp., 966–969 (2008).
13. K. E. Thomenius, "Evolution of Ultrasound Beamformers," Proc. IEEE Ultrason. Symp. **2**, 1615–1622 (1996).
14. J. A. Jensen and N. B. Svendsen, ""Calculation of pressure fields from arbitrarily shaped, apodized, and excited ultrasound transducers," IEEE Trans. Ultrason., Ferroelec, Freq. Contr. **39**(2), 262–267 (1992).
15. M. A. Lediju Bell, N. P. Kuo, D. Y. Song, J. U. Kang, and E. M. Boctor, "In vivo visualization of prostate brachytherapy seeds with photoacoustic imaging," J. Biomed. Opt. **19**(12), 126011 (2014).
16. M. A. Lediju Bell, X. Guo, D. Y. Song, and E. M. Boctor, "Transurethral light delivery for prostate photoacoustic imaging," J. Biomed. Opt. **20**(3), 036002 (2015).
17. L. Xi, G. Zhou, N. Gao, L. Yang, D. A. Gonzalo, S. J. Hughes, and H. Jiang, "Photoacoustic and fluorescence image-guided surgery using a multifunctional targeted nanoprobe," Ann. Surg. Oncol. **21**(5), 1602–1609 (2014).
18. M. A. Lediju Bell, A. K. Ostrowski, K. Li, P. Kazanzides, and E. M. Boctor, "Localization of Transcranial Targets for Photoacoustic-Guided Endonasal Surgeries," Photoacoustics **3**(2), 78–87 (2015).
19. A. Cheng, H. J. Kang, H. K. Zhang, R. H. Taylor, and E. M. Boctor, "Ultrasound to video registration using a bi-plane transrectal probe with photoacoustic markers," Proc. SPIE **9786**, 97860J (2016).
20. W. Xia, D. I. Nikitichev, J. M. Mari, S. J. West, R. Pratt, A. L. David, S. Ourselin, P. C. Beard, and A. E. Desjardins, "Performance characteristics of an interventional multispectral photoacoustic imaging system for guiding minimally invasive procedures," J. Biomed. Opt. **20**(8), 086005 (2015).
21. N. Dana, L. Di Biase, A. Natale, S. Emelianov, and R. Bouchard, "In vitro photoacoustic visualization of myocardial ablation lesions," Heart Rhythm **11**(1), 150–157 (2014).
22. M. L. Li, H. E. Zhang, K. Maslov, G. Stoica, and L. V. Wang, "Improved in vivo photoacoustic microscopy based on a virtual-detector concept," Opt. Lett. **31**(4), 474–476 (2006).
23. Y. Tsunoi, S. Sato, R. Watanabe, S. Kawauchi, H. Ashida, and M. Terakawa, "Compact acoustic-resolution photoacoustic imaging system with fiber-based illumination," Jpn. J. Appl. Phys. **53**(12), 126701 (2014).
24. H. K. Zhang, K. Kondo, M. Yamakawa, and T. Shiina, "Coded excitation using periodic and unipolar M-sequences for photoacoustic imaging and flow measurement," Opt. Express **24**(1), 17–29 (2016).

1. Introduction

Photoacoustic (PA) imaging is an important tool for various clinical and pre-clinical applications [1], providing functional information by visualizing optical absorption properties, and offering great synergy with conventional ultrasound imaging, which delineates anatomical structures. In order to construct a PA image, it is necessary to receive signals from different locations through scanning. While various scanning strategies are considered, the ultrasound array transducer can be regarded as the most accessible receiver because it is widely used in the clinic for ultrasound imaging [2–4]. In addition, receiving PA signals from the same ultrasound imaging array simplifies fusion of PA and ultrasound images [5].

When forming PA images, acquiring pre-beamformed channel data is essential because typical clinical ultrasound systems only provide access to delay-and-sum beamformed data [2,6]. Accessing pre-beamformed channel data requires custom hardware and parallel beamforming software, and is available for a limited number of research ultrasound platforms with dedicated channel data acquisition devices such as the Ultrasonix DAQ system [7]. These systems are generally expensive with fixed data transfer rates that prohibit high frame-rate, real-time imaging [8]. More importantly, most clinical ultrasound systems do not offer PA beamforming which hinders clinical transition. Harrison *et al.* [9] studied this issue and suggested changing the speed of sound parameter of clinical ultrasound systems. However, software access to change the speed of sound is not common and when available, the range for this change is limited, making this option insufficient for PA beamforming. In addition, this concept is limited to linear arrays, because angled beams (e.g. as in curvilinear arrays) alter the geometry of beamformer, as well as the speed of sound. Thus, it is not possible to compensate by simply changing the speed of sound. In contrast, post-beamformed radio frequency (RF) data is readily available with several clinical and research ultrasound platforms, thus to broaden the impact of clinical PA imaging, our goal is to devise a new PA image reconstruction approach based on ultrasound RF data that has already been beamformed by the system.

Biomedical Optics EXPRESS

We therefore propose a synthetic-aperture based beamforming algorithm, named Synthetic-aperture based PhotoAcoustic RE-beamforming (SPARE), utilizing ultrasound post-beamformed RF data as the pre-beamformed data for PA beamforming. When receive focusing is applied in ultrasound beamforming, the focal point can be regarded as a virtual element [10–12] to form a set of pre-beamformed data for PA beamforming. The SPARE beamformer takes the ultrasound data as input, and reconstructs a PA image with the correct focal delay.

In this paper, we first introduce the theory of the synthetic aperture based PA beamformer. Then, the resolution and signal-to-noise ratio (SNR) of the proposed method are evaluated through simulation, and an experiment is conducted to validate its feasibility. Finally, the limitations and the potential applications of this algorithm are discussed.

2. Theory

2.1 Ultrasound beamforming

In ultrasound image reconstruction, the delay function in delay-and-sum beamforming is computed from the distance between receivers and the target [13]. The acoustic wave is first transmitted from the ultrasound transducer, through a medium with a specific velocity, reflected at boundaries with impedance mismatching, and the backscattered sound is received by the ultrasound transducer. The entire acoustic time-of-flight (TOF) during this process can be formulated as,

$$t_{US}(r_F) = \frac{1}{c}\left(|r_T| + |r_R|\right), \tag{1}$$

where r_F is the focus point originating from the ultrasound image coordinates, r_T is the vector from the transmit element to the focal point, r_R is the vector from the focal point to the receive element, and c is the speed of sound. In clinical ultrasound systems, sequential beamforming with dynamic focus or fixed focus is generally applied as a delay-and-sum algorithm. In dynamic focusing, the axial component z_F of the focusing point varies with depth, while a single fixed depth focus is used for the fixed focusing.

The acoustic TOF of PA signals is half of that of ultrasound, because the acoustic wave is generated at the target by absorbing light energy, and the optical transmission side of time travel is negligible. Therefore, the acoustic TOF for photoacoustic imaging becomes

$$t_{PA}(r_F) = \frac{|r_R|}{c}. \tag{2}$$

Considering the differences between Eqs. (1) and (2), when beamforming is applied to the received PA signals based on Eq. (2), the beamformed RF signals are defocused, as shown in Fig. 1(a).

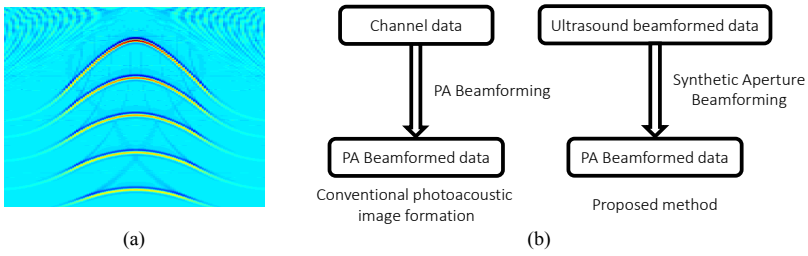

Fig. 1. (a) Example of ultrasound beamforming for photoacoustic signals. When five point targets are placed, the points are extended with orbits in the reconstructed image due to incorrect delays. (b) Diagram of proposed synthetic aperture beamforming.

Biomedical Optics EXPRESS

2.2 Synthetic-aperture based re-beamforming

In the SPARE beamforming, the beamformed RF data from the ultrasound scanner is not considered as defocused useless data, but as pre-beamformed RF data for PA beamforming. The additional delay-and-sum step is applied on the beamformed RF data, and the new photoacoustically beamformed RF data can be reconstructed. When fixed focusing is applied in the ultrasound beamforming process, the focus point in the axial direction is constant with depth, indicating that ideal focusing was applied at the specific focal depth with defocused signals appearing elsewhere. Starting from the single focal depth, the defocused signals appear as they were transmitted from the focal point (i.e. a virtual element as illustrated in Fig. 2b). In this sense, the ultrasound post-beamformed RF data is regarded as PA pre-beamformed RF data. For convenience, we define the ultrasound beamforming with a fixed focus as the first beamforming, and the following SPARE beamforming as the second beamforming. The TOF from the virtual element, when a fixed focus at z_F is applied, becomes

$$t\left(r_F'\right)=\frac{\left|r_R'\right|}{c}, \tag{3}$$

where

$$\left|r_R'\right|=\sqrt{\left(x_R\right)^2+\left(z_R-z_F\right)^2}, \tag{4}$$

and $r_F'=r_F-z_F$. x_R and z_R is the lateral and axial components of r_R, respectively. The dynamic receive delay function will be applied in the positive axial direction when $z_R \geq z_F$, and negative dynamic focusing delay will be applied when $z_R < z_F$. The diagrams in Fig. 2(b) and Fig. 2(c) show the re-beamforming process of the SPARE beamformer. Post-beamforming processes such as envelope detection and scan conversion will be applied on the reconstructed data for the PA image display.

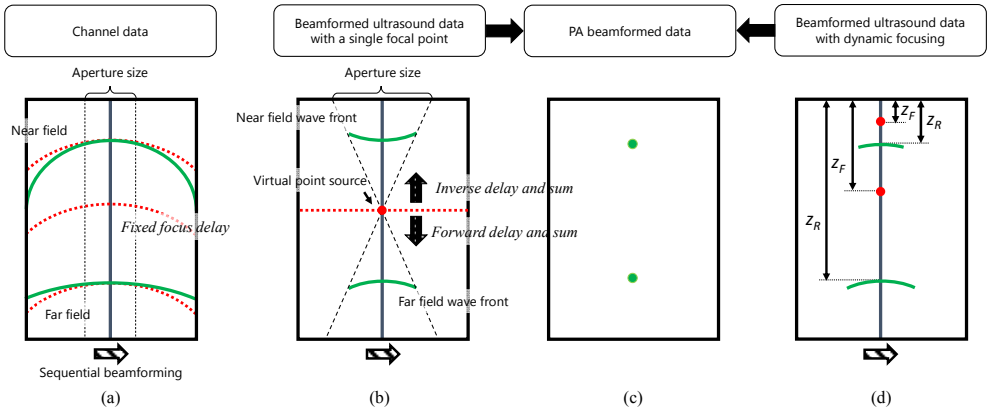

Fig. 2. Illustration of channel data and the SPARE beamforming process. (a) In channel data, the wave front of receive RF signals expands corresponding to the depth (green line). The red lines indicate fixed focus delay function. (b) When fixed receive focusing is applied, the delay function is only optimized to the focus depth (red line). (c) As a result of fixed receive focusing, the focal point can be regarded as a virtual point source, so that inverse and forward delay and sum can be applied. (d) Similarly, dynamic focusing could be regarded as a specific case of that in which the virtual element depth z_F is the half distance of re-beamforming focal depth z_R.

Although derived for fixed focusing, this theory is applicable to both fixed and dynamic focused beamformed ultrasound RF data with the primary difference being that in dynamic focusing, the round trip distance between the transmitter and the reflecting point in

Biomedical Optics EXPRESS

conventional ultrasound imaging must be considered along with the location of the virtual point source. Thus, in SPARE beamforming of dynamically focused data, we consider the virtual point source depth, z_F, to be dynamically varied by half of the photoacoustic beamforming focal point depth, z_R, as illustrated in Fig. 2(d). Note that $z_R = 2z_F$ is always true in this special case.

2.3 Resolution and SNR

The lateral resolution of photoacoustic imaging is proportional to the f-number, which is the ratio of aperture size to the focusing depth. In PA beamforming, the relationship between f-number ($F\#$) and lateral resolution can be described as

$$\text{Lateral Resolution} \propto \frac{F}{D} = F\#, \tag{5}$$

where F is focusing depth and D is the aperture size. Therefore, to achieve a high resolution PA image, a low f-number (i.e. a small focusing depth and/or a large aperture) is desired. In ultrasound imaging, the frequency of the received signals is another factor that affects the lateral resolution, which typically depends on the probe bandwidth in PA imaging.

In the proposed SPARE beamformer, four factors are involved to determine the lateral resolution: 1) the fixed focal depth z_F, 2) the SPARE beamforming focal depth z_R, 3) the fixed focus aperture size D_{US}, and 4) the aperture size for the SPARE beamforming D_{SA}. The fixed focus depth and aperture size are determined by the ultrasound system as in conventional beamforming, and the SPARE beamforming parameters are determined based on the fixed focus parameters, as discussed in Section 2.4.

The effective focusing depth and aperture of the SPARE beamformer, which defines the resolution of the reconstructed PA image, is

$$F_{SA} = \left| z_F - z_R \right|, \tag{6}$$

where z_F is considered as a virtual element point source, and the new focusing depth is computed starting from the virtual element.

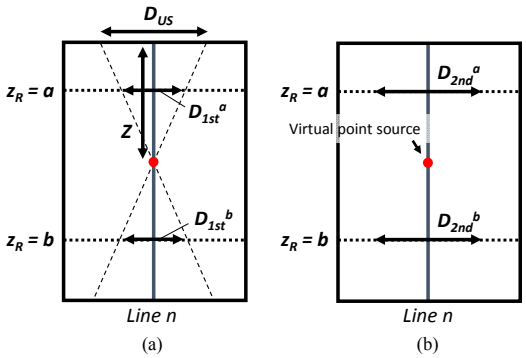

Fig. 3. The beamforming geometry when line n is beamformed. (a) The effective aperture size of the first beamforming is defined as $D_{1st}{}^a$ and $D_{1st}{}^b$ when $z_R = a$ and $z_R = b$ is chosen, respectively. (b) The effective aperture size of the second beamforming (SPARE) is defined as $D_{2nd}{}^a$ and $D_{2nd}{}^b$ when $z_R = a$ and $z_R = b$ is chosen.

The effective aperture size of the system is determined by both fixed focusing and the following second SPARE beamforming. For the fixed focusing, the effective aperture size in the first focusing step is affected by the fixed-focus aperture size and depth as illustrated in the geometrical region covered by dotted lines in Fig. 3. The effective aperture size in the first ultrasound beamforming is

Biomedical Optics EXPRESS

$$D_{1st} = \frac{D_{US} F_{SA}}{z_F}, \tag{7}$$

and that in second beamforming is

$$D_{2nd} = D_{SA}. \tag{8}$$

The overall effective aperture size is the smaller of the two apertures for the first or the second beamforming step. Hence, the overall effect on lateral resolution can be expressed as

$$\text{Lateral Resolution} \propto \begin{cases} \dfrac{F_{SA}}{D_{1st}}, & \text{if } D_{2nd} < D_{1st} \\ \dfrac{F_{SA}}{D_{2nd}}, & \text{if } D_{2nd} \geq D_{1st} \end{cases}. \tag{9}$$

The SNR is another factor that represents the quality of beamforming defined as

$$SNR = 20 \log_{10} \left\{ \frac{|A_{Max}|}{\sigma_{noise}} \right\}, \tag{10}$$

where A_{Max} is the maximum signal amplitude, and σ_{noise} is the RMS electrical noise level. The SNR of ultrasound signals depend on many factors including f-number, attenuation, reflection, and angle sensitivity of elements, etc. However, when all parameters except f-number are fixed, the SNR is determined based on f-number as

$$SNR = f(F\#). \tag{11}$$

In the proposed algorithm, therefore, Eq. (9) determines SNR as well as lateral resolution.

2.4 Optimum aperture size

The appropriate aperture size in the SPARE beamforming can be determined by the effective aperture size in the first ultrasound beamforming. As the resolution is determined by the aperture size used for fixed focusing, using a wider aperture in the second SPARE beamforming than the original aperture size from fixed focusing is unnecessary and does not provide additional resolution. Therefore, the optimum aperture size for the second SPARE beamforming can be calculated based on the first beamforming aperture size. The aperture size for the SPARE beamforming is defined as

$$K(z_R) = \frac{(|z_R - z_F|) D_{US}}{z_F}. \tag{12}$$

3. Methods

3.1 Simulation setup

Various center frequency signals were simulated using Field II [14], and N-shape waveforms with different absorber sizes were simulated to evaluate their effects on different impulse responses. For the resolution and SNR analyses, five photoacoustic point sources were placed at 10 mm, 20 mm, 30 mm, 40 mm, and 50 mm depth, respectively to observe the proposed re-beamforming effect at different target depths. Beamforming with a fixed focal point at 20 mm depth and dynamic focusing was applied to the simulated channel data, then the SPARE beamforming algorithm was applied. The center frequency of the impulse response was 2 MHz. A 128-element, 0.3 mm pitch, linear array transducer was assumed to be a receiver, which matches the setup of the experiment described in section 3.2. The received signals were sampled at 40MHz. We varied the following parameters: the fixed focal depth, the SPARE

Biomedical Optics EXPRESS

beamformer focal depth, the fixed focusing aperture size, and the aperture size for the SPARE beamforming. To provide a ground-truth resolution value for this setup, the conventional delay-and-sum PA beamforming algorithm was applied to the simulated channel data. The full-width at half maximum (FWHM) was calculated to evaluate the resolution of the beamforming algorithm. For the SNR analysis, –20 dB Gaussian noise compared to the maximum intensity was added to the background, and the SNR was computed using Eq. (10).

3.2 Experiment setup

The experimental setup is shown in Fig. 4. A 905 nm wavelength pulsed laser diode (PLD) (Laser Components) was used to irradiate a plastisol phantom with black ink. The diode laser was triggered by a function generator which was programmed through a PC. Since the light was absorbed by the surface of the phantom because of the high absorption coefficient of the black ink, PA signals could be generated from a tiny spot in the phantom, which could be regarded as a point source. The PLD is placed approximately 5 mm from the phantom surface, and the laser spot size at the incident surface was 1mm. PA signals were generated at from the surface of the phantom and traveled toward the ultrasound probe, located on the opposite surface of the phantom. The generated PA signal was received by a 0.3 mm pitch, 128-element, linear array ultrasound transducer. The received channel data were transferred to a channel data collection device (Sonix DAQ) via a clinical ultrasound machine (Sonix Touch, Ultrasonix), and saved to the PC. Beamforming algorithms were applied to the acquired channel data.

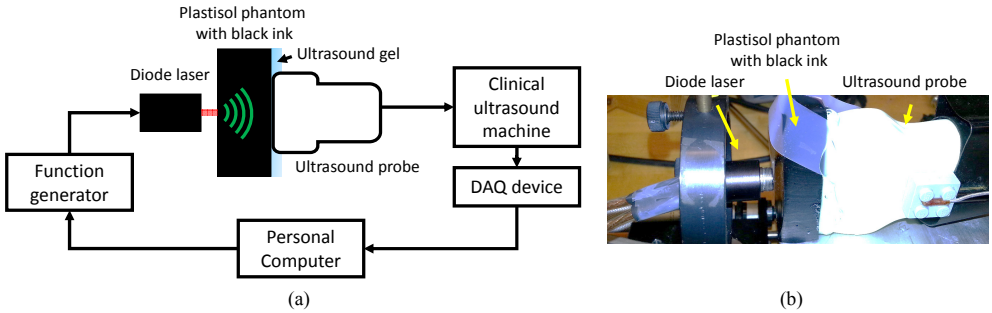

Fig. 4. (a) Experimental setup diagram. (b) Picture of the setup.

4. Results

4.1 Simulated waveform and images

Simulated waveforms and the resulting reconstructed PA images using channel data (center) and ultrasound beamformed RF data with a fixed focal point (right) are shown in Fig. 5.

The true PA signals from a cyliderical target is N-shape, and Figs. 5(a) and 5(b) shows the waveform when the absorber size was set to 1 mm and 0.5 mm, respectively. However, the ultrasound receiver is generally band-limited with a specific center frequency. When the PA signals are received by the ultrasound probe, the PA signals will be filtered at the probe's center frequency. Figures 5(c) and 5(d) demonstrate signals with center frequencies of 2 MHz and 5 MHz, respectively. The maximum available aperture size was used for all reconstructed images. PA images using the proposed SPARE beamformer were similar to that from conventional PA beamforming from raw channel data. These results indicate that our algorithm is independent of the impulse responses determined by the absorber size and the ultrasound probe.

Biomedical Optics EXPRESS

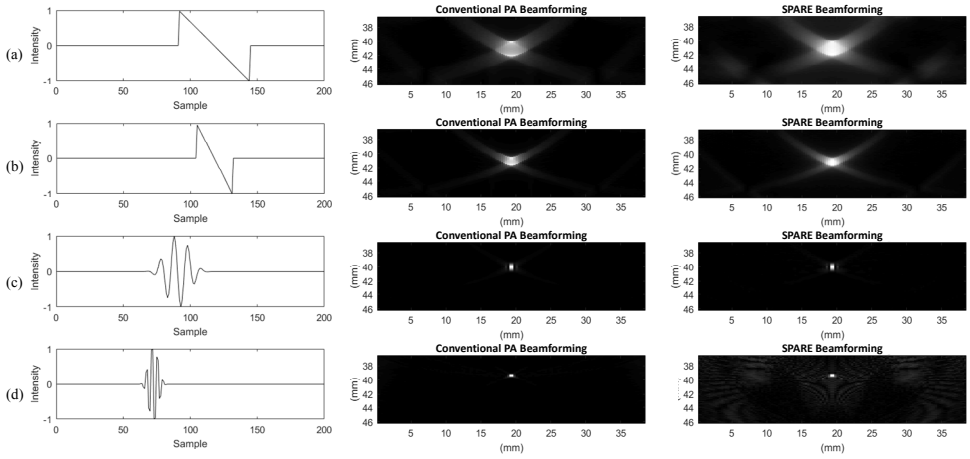

Fig. 5. Simulated photoacoustic waveforms, PA images from channel data, and PA images using SPARE beamformer are shown. Fixed focusing at 20 mm depth was used for SPARE beamforming. (a) 1 mm and (b) 0.5 mm diameter objects with N-shape impulse responses were simulated. For a point source, (c) 2 MHz, (d) 5 MHz center frequency waves were simulated assuming that a band-limited ultrasound transducer was used to receive these signals.

4.2 Resolution evaluation

To quantitatively evaluate the performance of the proposed SPARE beamformer, the resolution of reconstructed point targets was compared to the theoretical property introduced in Section 2.3. We first analyzed the FWHM of the PA point reconstructed with conventional delay-and-sum beamforming for each depth as a function of aperture size. In this simulation, the full aperture was used for the PA beamforming to estimate the maximum achievable resolution. As shown in Fig. 6(c), for conventional delay-and-sum photoacoustic beamforming, the FWHM decreased as the target depth decreased and the aperture size increased. In addition, the FWHM was evaluated as a function of f-number. For those data, the metric of f-number was computed for corresponding depth and aperture size using Eq. (5), and we present the average of FWHM values for the corresponding f-number [Fig. 5(d)]. This rearranged result was used as the ground truth control to compare with the proposed method.

Figures 6(a) and 6(b) show the resolution of SPARE beamformed images. When the first beamforming aperture was varied, the second beamforming aperture used all elements [Fig. 6(a)]. Similarly, when the second beamforming aperture was varied, the maximum available aperture size was used in the first beamforming [Fig. 6(b)]. Figure 6(a) shows the decrease of FWHM corresponding to the aperture size increase and the fixed focal depth reduction, and Fig. 6(b) shows the FWHM reduction due to the aperture size increase in the second beamforming step. These SPARE beamforming results were rearranged based on the f-number of each depth and aperture size, and the FWHM value was compared to that of the ground truth values presented in Fig. 6(c). Figure 6(d) shows the result of this comparison for various f-numbers. The resolution of the proposed method agrees well with the ground truth values with a correlation coefficient of 99.87%.

Biomedical Optics EXPRESS

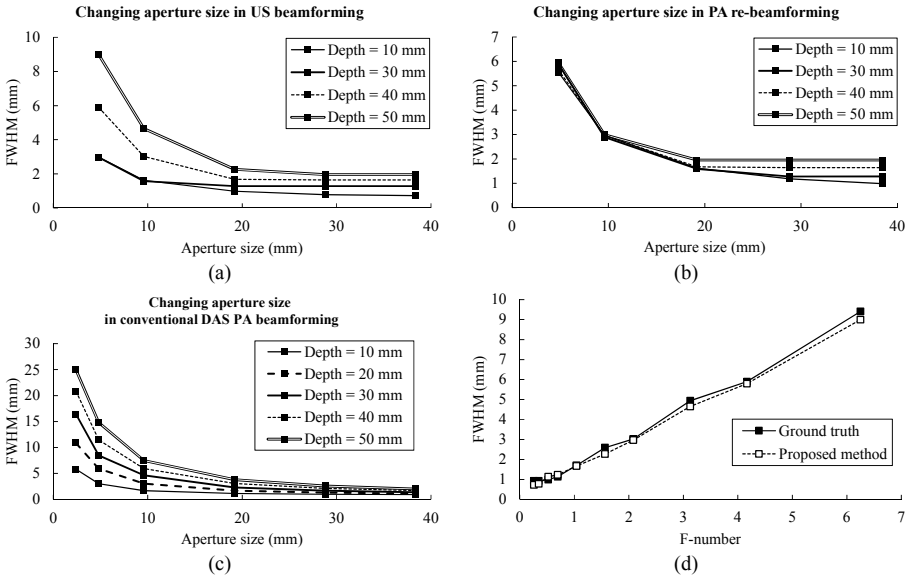

Fig. 6. The FWHM of the proposed re-beamforming for the designated focusing depth, and varying the aperture size in the (a) first beamforming and (b) the second beamforming. (c) The ground truth FWHM results using a delay-and-sum algorithm with dynamic focusing. (d) The focusing depth and aperture size parameters in Figs. 6a-c were compressed into the metric of f-number. The theoretical ground truth values were computed by fitting the ground truth data from Fig. 6(c) into Eq. (5).

4.3 SNR evaluation

Following the evaluation scheme used in Section 4.2, the SNR of simulated beamformed data using the conventional PA beamformer and proposed re-beamforming algorithm were calculated using Eq. (10) [Figs. 7(a)-7(b)]. For the proposed method, the aperture size was changed for either the first or second beamformer; when one was changed, the other aperture size was fixed to be the maximum aperture size [Fig. 7(a)]. The ground truth data was based on conventional PA beamforming by changing the aperture size and the focal depth [Fig. 7(b)]. To observe the characteristics of SNR for a corresponding f-number, the SNR at a f-number of 1.04 was normalized to be 0 dB throughout different target depth results. The comparison with ground truth is shown in Fig. 7(c). A shared trend could be seen between the proposed method and ground truth values, and the correlation coefficient obtained from comparison of the two plots in Fig. 7(c) was 91.56%. One difference between the results for SNR [Fig. 7(c)] and resolution [Fig. 6(d)] is that the SNR is not solely proportional to the f-number, likely because other factors (e.g. attenuation difference at different depths) also affect the SNR.

Biomedical Optics EXPRESS

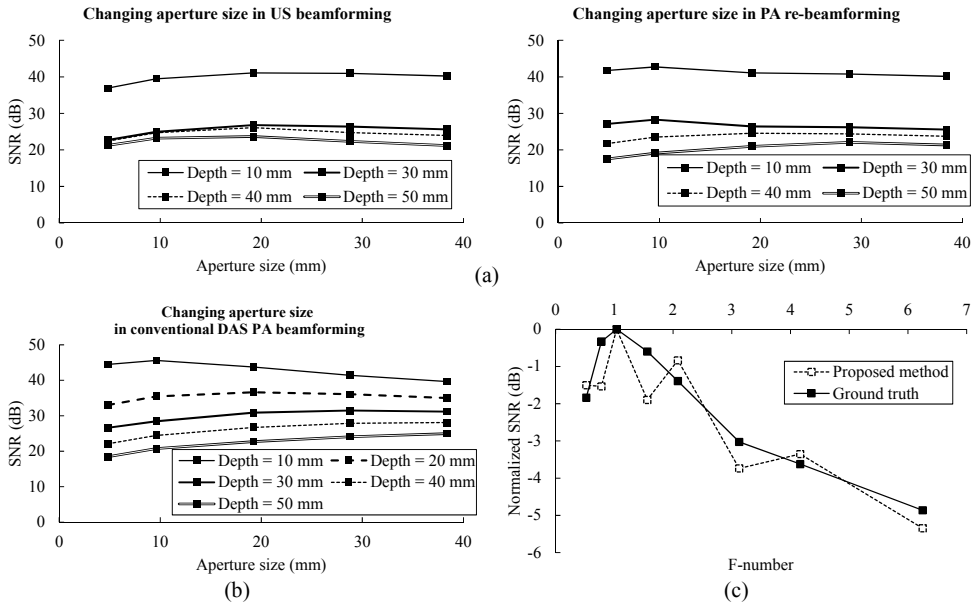

Fig. 7. (a) The measured SNR of proposed beamformer varying the aperture size in the first beamforming (left) and the second beamforming. One beamformer aperture size was fixed to be maximum when the other aperture size was varied. (b) The ground truth SNR results using a delay-and-sum algorithm with dynamic focusing. (c) The focusing depth and aperture size parameters in Figs. 7(a)-7(b) were compressed into the metric of f-number. To compensate the SNR variance for the same f-number but different target depth, the SNR of f-number 1.04 was normalized to be 0 dB. The theoretical ground truth values were computed by fitting the ground truth data from Fig. 7(b) into Eq. (9).

4.4 PA re-beamforming for dynamically focused beamformed ultrasound RF data

Figure 8 shows the reconstructed results of SA beamforming using dynamically focused beamformed ultrasound RF data, displayed with a dynamic range of 30 dB. The defocused beamformed ultrasound data was re-beamformed through SPARE beamforming. Comparing the proposed method with the conventional PA beamforming (Fig. 8(a)), a similar sidelobe level is observed, while unique artifacts are visible in the SPARE beamformed results (Figs. 8(b)-8(c)). The aperture size for the ultrasound beamforming was changed from 128 elements (Fig. 8(b)) to 16 elements (Fig. 8(c)). The point targets obtained with the ultrasound beamforming step were not only degraded due to incorrect delay functions, but a large grating lobe also appeared in the near field when a large aperture was used in ultrasound beamforming step. This grating lobe artifact remains in the SPARE beamforming result (Fig. 8(b)). When a smaller aperture was used in ultrasound beamforming, the grating lobe artifacts were mitigated, and therefore were less visible in the corresponding SPARE beamformed image (Fig. 8(c)). On the other hand, when a small aperture size was employed, the resolution of the deeper point targets were degraded compared to that obtained with the larger aperture. Thus, in the practical implementation, one solution to overcome these challenges to optimize image quality is a variable aperture size (e.g. fixed f-number throughout the image with a smaller aperture size in the near region and a larger aperture size in the far region).

Biomedical Optics EXPRESS

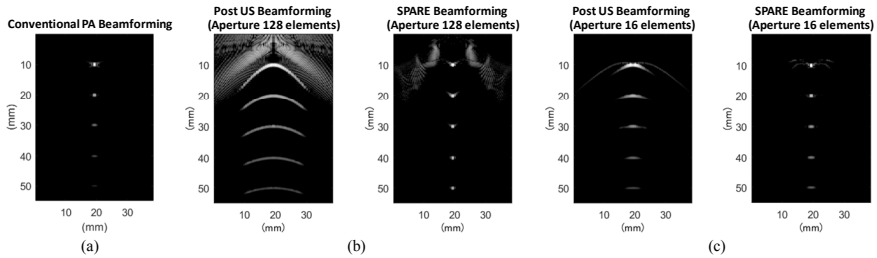

Fig. 8. (a) The reconstructed PA image from channel data as a ground truth. (b-c) The reconstructed images through ultrasound and SPARE beamforming. Dynamic focusing is applied as ultrasound beamforming. Grating lobe artifacts are visible in the near field of ultrasound beamforming result (b) when a large aperture is used in 1st ultrasound beamforming, but it is drastically reduced when a small aperture size is used (c).

4.5 Experimental evaluation

Ultrasound beamforming with fixed focusing and dynamic focusing was applied to experimental channel data to produce two types of ultrasound post-beamformed data. The experimental SPARE beamformer results from ultrasound beamforming with a single focal point are shown in Fig. 9, displayed with 20 dB dynamic range.The point source located at 12 mm was reconstructed for all fixed foci in the range of 3 mm to 45 mm. The FWHM and SNR of the point source was measured for different fixed focal depths in Fig. 9(c). The results of conventional PA beamforming using channel data is also shown as the ground truth. This ground truth result can be regarded as the lower boundary of achievable FWHM for these data because the maximum available aperture information is used. For SPARE beamforming results, the FWHM was similar to that of the ground truth when the fixed focusing was applied from 9 mm to 21 mm. However, the reconstructed point was degraded in the lateral direction when the fixed focal depth was far from the target. This degradation is likely due to an insufficient aperture size for the first and the second beamforming steps. In terms of SNR, a similar trend of image quality improvement was observed compared to the ground truth result, and the fixed focal depth over 21 mm shows a better SNR.

Figure 10 shows the experimental SPARE beamforming results from dynamically focused ultrasound beamforming. The defocused target in ultrasound post-beamformed result was re-focused with SPARE beamforming.

5. Discussion

Generally, the simulation results presented in this manuscript have good agreement with theory, and the proposed method produces similar resolution and SNR to that obtained with conventional delay-and-sum beamforming. The agreement between the theory and simulation for SNR was influenced by multiple confounding factors, additionally evidenced by the SPARE beamformer showing a better SNR compared to conventional PA beamforming in the experimental results [Fig. 9]. Theoretically, the SNR of both beamformers should be similar, and this discrepancy could be attributed to summing axially distributed coherent information twice, once for each beamforming step. If the waveform is not a simple point target, the axial components from the non-point wavefront are first summed during ultrasound beamforming. This accumulated information would be further summed after SPARE beamforming. When the SNR of the channel signals is significantly low, the reconstructed image may contain a noise-related gradation artifact as the number of summations varies for each focal point. Hence, beamforming with the full aperture is more appropriate in this high-noise case.

Biomedical Optics EXPRESS

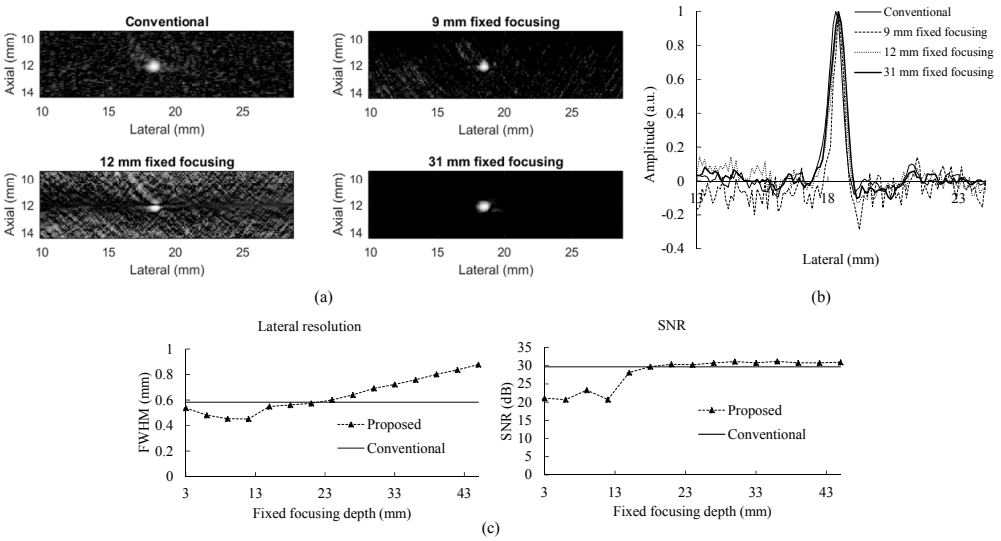

Fig. 9. Experimental SPARE beamforming results. (a) Reconstructed photoacoustic images of conventional dynamic focusing for channel data, 9 mm, 12 mm, and 31 mm fixed focal depths. (b) Lateral profile of the point target. (c) Measured FWHM and SNR for various fixed focal depths.

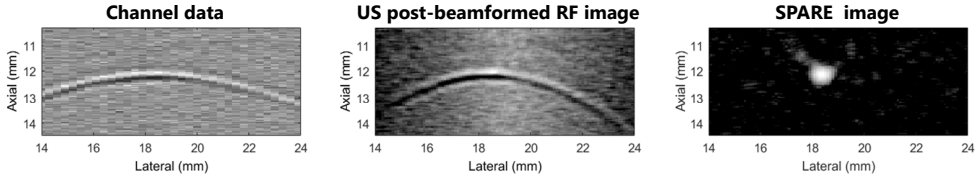

Fig. 10. Experimental SPARE beamforming results with dynamic focusing. Original channel data, intermediate ultrasound post-beamformed result, and final SPARE post-beamformed result are shown from left to right, respectively. The dynamic range of 20 dB was used for display.

When fixed focusing is used as the ultrasound beamforming, the fixed focal depth should not be the same as the interested target location, as near field artifacts would appear as seen in Fig. 9(a) (compare 12 mm fixed focus result to 9 mm and 31 mm fixed focus results). Moreover, a deep fixed focal depth is desired to keep stable SNR, however, this depth should be sufficiently shallow to avoid degradation of the resolution, as demonstrated in the experimental results shown in Fig. 9(c). Dynamic focusing does not have this problem as the ultrasound focal depth is always shorter than the ideal PA focal depth.

A superiority of the proposed method over the speed of sound adjustment approach [9] is the generality to steered beams (e.g. phased arrays) or to beam geometries that differ from those of the linear array (e.g. curvilinear arrays). As formulated in Eqs. (3) and (4), the proposed beamformer applys a delay-and-sum assuming the PA signals are received at the virtual element. Therefore, even if the ultrasound beam is angled, the delay-and-sum algorithm can still be applied with the virtual element created by the angled beam.

We expect that image quality improvement strategies (apodization, transmit gain compensation, etc.) will have a similar effect on the improvement of SPARE images. The effect of the beamformer for specific f-number parameter is shown and discussed in simulation. Apodization could improve the appearance of the reconstructed image, because it reduces the sidelobes in the ultrasound beam.

Biomedical Optics EXPRESS

The effect of speed of sound variations with SPARE beamforming is expected to be similar to that of conventional PA beamforming if the same speed of sound is utilized for both ultrasound (1st beamformer) and SPARE beamforming. However, the SPARE beamformer has the added advantage of compensating for the incorrect speed of sound utilized during the ultrasound beamforming step by considering the true focal depth and speed of sound during the SPARE beamforming. This is, however, not possible if the speed of sound varies widely throughout the medium being imaged.

Although image formation was demonstrated with point-like targets throughout this manuscript, the SPARE beamformer has potential to be implemented to visualize any structure that has a high optical absorption property. Thus, the key contribution of the proposed SPARE algorithm is its potential for integration into real-time imaging systems using clinical ultrasound machines. Currently, most real-time photoacoustic imaging systems are based on open platform research systems [7]. However, the option to use an FDA-approved clinical ultrasound system eases the transition of photoacoustic technology into the clinic. Potential applications include real-time in vivo photoacoustic visualization for brachytherapy monitoring [15,16], image-guided surgery [17,18], interventional photoacoustic tracking [19], multispectral interventional imaging [20], and cardiac radiofrequency ablation monitoring [21].

A high pulse repetition frequency (PRF) laser system is one system requirement for the SPARE beamformer. Since the ultrasound post-beamformed RF data acquisition relies on a clinical ultrasound system, it is necessary to synchronize the laser transmission to the ultrasound line transmission trigger. To maintain similar frame rates to that of conventional ultrasound B-mode imaging, the PRF of the laser transmission should be the same as that of the ultrasound transmission frequency. Therefore, a high PRF laser system, like the PLD used in this paper, is desirable. Ultrasound transmission suppression can be considered as another system requirement. Turning off the transmit events is the most ideal solution. However, if this feature is unavailable, an alternative is to reduce the voltage of the transmission energy. Another approach is to use an electric circuit to control the laser transmit timing. The PA signals would be highlighted by subtracting the images with and without laser excitation.

In addition to enable broader use of PA imaging through clinical systems, the SPARE beamformer applied to fixed focus data is also applicable to PA tomogram formation using a hydrophone combined with an acoustic lens with a focal point, as proposed by Li et al. [22]. Hydrophones are widely used as a PA signal receiver because of its wide frequency receiving capability and sensitivity compared to a clinical ultrasound array [23]. PA tomograms can be formed by sweeping the hydrophone using a Cartesian stage. Although large-diameter hydrophones have high sensitivity, their wide reception angles cause suboptimal lateral resolution [24]. Attaching an acoustic lens is a simple solution to provide a focus, but the higher resolution made possible by this lens is only available near the focal point, and the image is defocused outside of the focal point. The acoustic lens focuses the acoustic beam for a single depth, which is the same situation for the fixed beamformed data using a linear array. Thus, the proposed algorithm could be a solution to provide an opportunity to generate a dynamically focused PA tomograms with SPARE beamforming of the received data.

6. Conclusion

In this paper, we propose a synthetic-aperture based PA beamforming method utilizing ultrasound post-beamformed RF data. The goal is to reconstruct PA images utilizing data that can be acquired from any clinical ultrasound machine. The theoretical basis for quantifying the image resolution is introduced, and it is validated with simulations. As a result, it is possible to estimate the potential image resolution and SNR of this beamformer under various parameter definitions. In addition, we conducted a phantom experiment to beamform a point source using the SPARE beamformer. Results demonstrate the feasibility of the algorithm

Biomedical Optics EXPRESS

under practical data acquisition. Future work includes implementing the algorithm in real-time.

Acknowledgments

Financial supports were provided by Johns Hopkins University internal funds, NSF Grant No. IIS-1162095, NIH Grant No. R21CA202199, and NIBIB-NIH Grant No. EB015638. M.A. Lediju Bell is supported by NIH grant K99 EB018994.